Etch pits on (hk0) and (hh) silicon surfaces. Experimental shapes and simulations

C.R. Tellier

Etch Pits on (hk0) and (hhℓ) Silicon Surfaces. Experimental Shapes and Simulations

C.R. Tellier

FEMTO-ST Institute, Frequency and Time Department,
26 chemin de l'épitaphe, 25030 Besançon Cedex, France

Email: ctellier@ens2m.fr
Tel : +33 (0)3 81 40 28 30, *Fax* : + 33 (0)3 81 88 57 14

Shortened title: **Etch Pits on (hk0) and (hhℓ) Silicon Surfaces. Experiments and Simulations**

PACS. 07.05.Tp Computer modelling and simulation - 81.05.Cy Elemental semiconductors- 81.65.Cf Surface cleaning, etching, patterning

Abstract

The present work is concerned with the development of etch pits on (hk0) and (hhl) silicon surfaces immersed in various etchants. Final shapes of small etch pits are found to be bounded by {111} facets solely. The orientation dependence of etching shapes is explained in terms of a kinematic and tensorial model involved in the simulator TENSOSIM. An agreement between experimental and theoretical etching shapes is observed showing that the simulator can generate quite accurate 3D etching shapes for pits blocked by limiting facets. After a fair adjustment of the database the simulator derives also etching shapes close to experimental shapes of large pits.

1 Introduction

Silicon is commonly used to fabricate by wet etching [1-6] micromechanical devices for sensors and actuators applications. KOH solutions are currently utilized [2-7] for the micromachining of silicon structures but other etchants [8-13] may be adopted. In the last decade TMAH based solutions [8-11] were found to be fully compatible with MOS circuit technology. Furthermore some recent works [12,13] were devoted to the chemical etching of silicon plates in NaOH etchants.

A chemically inert masking film is lithography opened to fabricate mesas and membranes on silicon surfaces. During the opening process some mask pitting may be produced. As a result this pitting gives rise to the formation of small etched holes during the subsequent micromachining. In the following these holes are called etch pits even if crystal imperfections and especially emergent dislocations [2,14] are not at the origin of etch pit formation.

Up to now simulations of etch pits formation are Monte Carlo simulations [15-17] that consider the atomic structure of the starting surface and assume that the probability of removing a certain atom of the surface is connected to the number of nearest neighbour atomic bonds. Most of these works [15,17] are concerned with Si(100) surfaces. Among these works some [16,17] focus on the Monte Carlo simulation of pyramidal etch hillocks that develop when silicate particles are deposited on the (100) surface during the etching process. Moreover to our knowledge no simulations treat the development of etch pits on (hk0) and (hhℓ) surfaces. In the present work we propose to derive theoretical shapes of etch pits with a simulation tool TENSOSIM [18-20] that is based on an analytical kinematic model.

Experimental shapes of etch pits produced on differently oriented silicon surfaces immersed in various anisotropic etchants are presented in the first part of this paper. The major conclusion of this first part is that the final shape of a small etch pit is solely orientation dependent. The nature of etchant has no influence on this final shape and consequently theoretical shapes can be derived by choosing a convenient etchant. So a database for the chemical etching of silicon in a KOH 35% solution is constructed in the second part. In the third part this database is introduced in the simulation tool TENSOSIM to furnish the orientation dependent shape of etch pits.

2 Experimental results

2.1 Experimental details

Thin (hhℓ) and (hk0) plates were cut from a p-type silicon ingot with an electrical resistivity in the range 1-30 Ωcm. Orientations as defined by the IEEE standard on Piezoelectricity [21] are listed in Table 1. With this standard the reference cut is the (010) surface. A (hk0) surface (or x'_1x_3 plane) is obtained by a single rotation of φ degrees about the x_3 axis (or [001] direction). Starting with the [110] surface (φ = – 45°) a second rotation of θ degrees about the rotated x'_1 axis ($[1\bar{1}0]$ direction) generates a (hhℓ) surface (or $x'_1x'_3$ plane). The thickness of plates was approximately 500 µm. A two layer (silicon dioxide-silicon nitride) coating was applied on the upper face of plates. Combinations of circular masks were then patterned on this coating using conventional photolithography. Structures (membranes and mesa) were micromachined in various etchants (Table 2) at a constant temperature of 60°C. The etching duration was the same for all cuts immersed in a given solution. Moreover depending on orientation the etch depth was in the range 70 µm-120 µm. Etched surfaces were examined by Scanning Electron Microscopy. On SEM images of micromachined plates some etch pits due to mask pitting were depicted on the upper surface of mesas. In most cases the lateral sizes of these etch pits did not exceed 30 µm.

2.2 Experimental etch pits

Etch pits develop when the inert mask contains opened defects with concave contours. Let us first consider the case of a 35% KOH solution. The chemical etching of silicon in this KOH solution is governed by anisotropy of type 1 [5]. Both {100}, {110} and {111} planes are associated with protuberances of the dissolution slowness surface of equation $L(\varphi,\theta)$. The anisotropy ratio $k= L_{\{111\}}/L_{\{100\}}$ takes a value larger than 50 and {110} planes dissolve about twice rapidly than {100} planes. The {111} protuberances are very peaky and in the vicinity of {111} orientations the trajectories of surface elements diverge markedly at concave intersections. Consequently {111} facets limit in majority etched holes and etch pits of small size that are only bounded by {111} planes exhibit a top contour composed of successive linear segments LS_i. So etch pits on (010) surfaces are pyramidal with four {111} limiting facets. Figure 1 shows etch pits on (010) surfaces etched in NaOH and tetra-methyl ammonium hydroxide (TMAH) solutions. Here again the etch pits are limited by {111} facets and exhibit the characteristic pyramidal shape. We thus infer that the shape of etch pits is only determined by the orientation of the silicon surface provided the lateral size of mask defects remains small as compared with etch depth. In this condition the nature of etchant is irrelevant to shape of etch pits. This feature is conveniently illustrated by Figures 2 and 3 that show etch pits related to various (hk0) and (hhℓ) surfaces. Let us turn attention to SEM images 2a and 2A (Figure 2) related to (110) surfaces. Care must be taken that in the case of TMAH solution (image 2a) on the one hand the bottom (110) surface is still visible and that on the second hand an additional facet (f) participates to the concave part of etched pit. However the four {111} facets that make an angle of 35° with the [001] direction as well as the two {111} facets that intersect the (110) surface along the horizontal <110> direction can be easily identified.

As under the above specified conditions the nature of etchant does not affect the final shape of {hk0} and {hhl} etch pits we have collected in Figures 4 and 5 the SEM images of etch pits as provided by various etchants. All etch pits shown in these figures are bounded by {111} planes only. Turning attention to (hk0) planes we observe

i) The progressive evolution of shape characterized by the destruction of the pyramidal shape of (010) pits.

ii) A symmetrical development of {111} facets with respect to the x'_1 axis that constitutes the intersecting line of the (001) plane with the reference surface. Let us effectively recall that the (001) plane acts as a mirror plane.

Etch pits on (11ℓ) (Figure 5) deviate also more and more from the pyramidal etch pit when the angle of cut θ decreases from 80° to 58° (see Table 1). The mirror symmetry associated with the $(1\bar{1}0)$ plane gives now shapes with a symmetry with respect to the rotated x'_3 axis if we start with a defect having an appropriate contour (circular contour or rectangular contour aligned along x'_1 axis). Departure from the mirror symmetry as observed in Figure 5d may be attributed to more complex shape of the contour defect. We can also observe that limiting {111} facets are sometimes terraced (see Figures 5b, 5c and 5d for example). But other works [12,22] report also the presence of macrosteps on {111} surfaces. Etch pits that develop on (hh1) surfaces are collected in Figure 6. These etch pits exhibit moderate changes in shape with orientation in accord with the assumption that etch pits consist only of {111} facets. A simultaneous examination of Figures 5 and 6 reveals clearly that when a doubly rotated surface falls over from the (001) surface (θ=90°) to the (110) surface (θ=0°) the more significant change in shape occurs when we pass through the (111) surface. Effectively the two outward {111} facets (called f_{O3} and f_{O3}* in Figure 5) that contribute to (11ℓ) etch pits do not remain outward facets on the SEM images of (hh1) pits (Figure 6). Consider now

bordering f_{O1} and f_{O2} facets that intersect (11ℓ) and (hh1) surfaces along the $[1\bar{1}0]$ direction (Figures 5 and 6). The f_{O1} facet corresponds to the (111) facet whereas the second outward facet f_{O2} is identified as $(11\bar{1})$ facet and $(\bar{1}\bar{1}1)$ facet for (hh1) and (11ℓ) pits respectively. It is thus easy by simple geometrical considerations to calculate the lateral extent $LE_{\{111\}}$ of these two limiting facets. Let be $\alpha_{f_{O1}}$ and $\alpha_{f_{O2}}$ the inclinations of these facets with respect to the reference surface. Obviously the ratio of lateral extents $K_{LE} = LE_{f_{O1}}/LE_{f_{O2}}$ is:

$$K_{LE} = TAN\ \alpha_{f_{O2}}/TAN\ \alpha_{f_{O1}} \qquad (1)$$

For the (11ℓ) and (hh1) etch pits theoretical values of lateral extent ratio K_{LE} are collected in Table 3. Also given in Table 3 are experimental values of K_{LE} obtained by estimating the number of pixels on numeric SEM images. There is a good agreement between theoretical values for K_{LE} and experimental values. The largest deviation that reaches 8% is for the (221) surface. Departures for other reference surfaces remain in the range ±5%. Note that the evaluation of K_{LE} for (112) etch pits remains impossible because the $(11\bar{1})$ facet (facet f_{O2}) lies perpendicular to the reference surface. This feature is verified experimentally (see Figure 5).

As a conclusion of the experimental study we naturally argue that the formation of etch pits on (hhℓ) and (hk0) surface is independent of the nature of the etchant as long as etch pits are bordered solely by {111} facets. The final shape of etch pits can thus be constructed numerically using a database specific to one of etchants listed in Table 2. For this purpose in the following section:

i) The theoretical framework of the simulation is briefly introduced.
ii) The database related to 35% wt. KOH solution is adjusted.

3 Theoretical framework and database for 35% KOH

3.1 Theoretical framework

The numerical simulation is based on an analytical model of the anisotropic dissolution presented several years ago by Tellier [23,24]. This model called KT model (for kinematic and tensorial model) constitutes a 3D extension of the kinematic model originally proposed by Frank [25,26]. In the 3D model to take in account the anisotropy we attach a dissolution slowness vector $\mathbf{L}(\varphi,\theta)$ to a surface element $\mathbf{dS}(\varphi,\theta)$ of orientation (φ,θ). The dissolution slowness vector is defined in such a way that:

i) Its direction coincides with that of the unit inward normal $\mathbf{n}(\varphi,\theta)$ to the surface element.

ii) Its magnitude $L(\varphi,\theta)$ is equal to the reciprocal of the etch rate related to the surface element.

When the orientation of the surface element varies the dissolution slowness vector describes in space a representative surface called the dissolution slowness surface. The originality of the KT model is to adopt a tensorial formulation to express the analytical equation for the dissolution slowness surface. This formulation involves Cartesian components of $\mathbf{n}(\varphi,\theta)$ and dissolution constants. These dissolution constants are components of dissolution tensors and consequently classical tensor transformation rules are used to reduce the number of constants. As a result the equation for the dissolution slowness surface reflects naturally the symmetry elements of the point group related to the crystal into consideration.

To construct numerically the final shape of a micromachined structure it is necessary to follow the motion of starting surface elements within the crystal during the dissolution. Kinematic models [23,25,26] show that surface elements propagate along straight lines if the dissolution is governed solely by orientation. We thus need expression for the displacement vector $\mathbf{P}(\varphi,\theta)$ of a surface element. Fortunately the displacement **P** can be calculated [23] from the analytical equation for the dissolution slowness surface. Calculation of displacements **P** of all surface elements potentially present at the starting surface allows us to derive the final shape of structure provided some specific algorithms [27] were carried out in the simulation tool. The accord between simulated and experimental etching shapes is dependent on values of the dissolution constants as determined from experiments. Effectively the non zero dissolution constants compose the database of the simulator. A database for the 35% wt. KOH etchant and silicon crystal was proposed in a previous work [5]. Some departures between theory and experiment were observed showing that is necessary to perform additional adjustments. These adjustments are presented in the following section.

3.2 Adjustment of the database

To determine the database we follow a two step procedure described elsewhere [28]. In the first step we analyze experimental results related to:

i) The etch rate of differently oriented silicon surfaces.

ii) 2D etching shapes and especially out-of-roundness profiles that are representations of changes in the contour shape of starting circular plates.

However this analysis leads to deviations because:

i) Etched surfaces are covered by dissolution figures [12,29-31] and consequently measured etch rates differs more and less from the etch rate of a perfect planar surface.

ii) Thorough and faithful analysis of (hk0) and (hhℓ) out-of-roundness profiles furnishes with very good agreement orientations for which polar plots of the dissolution slowness $\mathbf{L}(\varphi,\theta)$ exhibit minima and maxima. But never the successive amplitudes of minima and maxima can be extracted with a good accuracy from experimental out-of-roundness profiles. So when the first step is terminated some uncertainties in the elaborated database remain. It is the reason why successive comparisons between experimental shapes and simulated 3D etching shapes as derived with the simulator TENSOSIM (see section 4.1.) are performed in the second step in order to elaborate an iterative adjustment of the database.

Several works have shown [5,10,12] that the adjustment of the dissolution constants is easier when we concentrate our study on simple structures such as membranes and mesas micromachined with a starting circular mask. Figures 7a and 7a* give examples of (hk0) "circular" membranes and mesas etched in a 35% wt. KOH solution. A previous database (Law 1, [5]) has been determined by applying only the first step of the procedure. Figures 7b and 7b* collect the theoretical shapes obtained using the Law 1. A recent adjustment of the database (New Law) furnishes the simulated structures of Figures 7c and 7c*. Note that taken into account the mirror symmetry only simulated half structures are drawn in Figure 7. Comparing theoretical shapes of membranes with experimental shapes we see at first sight roughly qualitative agreement for the two laws. However comparing theoretical mesas with the observed mesas several differences can be noticed:

(1) The top contour of theoretical mesas derived with the Law 1 are more rounded than contours of mesas simulated with the new database. This difference is particularly marked for the (230) mesa. Turning attention to the SEM image of this mesa (Figure 7a*) we observe that the upper contour is effectively composed of linear segments in agreement with the New Law simulation.

(2) Mesas in Figures 7a and 7a* are partly limited by slightly disorientated shoulders (such as shoulders S1, S2 and S3) that joint more vertical facets to the etched reference surface. Theoretical shapes corresponding to Law 1 have not evolved as experimental shapes. A very important difference is the absence of shoulders S2 and S3 on simulated mesas. Fortunately with the New Law shoulders S2 and S3 are formed in regions similar to experimental regions.

(3) Regions with bunching (see regions B1 and B2 in Figures 7a and 7a*) can be observed on the SEM images of mesas. Moreover in practice the convergence of facets may form bunching regions composed of terraces as shown by regions B1 and B2. At this point it is important to realize that simulations furnish only wrapping curves. Terraces or dissolution figures on etched surfaces are not incorporated in the simulation tool. Consequently comparison of theory and experiments focus essentially on identification of regions where bunching occurs. Comparison reveals that the New Law predicts convergence of facets in regions similar to observed regions.

So points (1) and (2) call for an adoption of the New Law to improve the simulation of theoretical shapes especially for mesas shapes. Effectively it is less easy to reproduce the adequate shape of an etched mesa because we are concerned simultaneously with concave intersections (beneath the mask) and with a convex top contour. Accordingly the testing of possible databases with simulated mesas is required. Hence Figure 8 furnishes additional comparison. Here again the New Law appears to be more optimal than the Law 1.

In conclusion for simulation of 3D etching shapes it is best to work with the database related to the New Law. This database is composed of dissolution constants of rank greater than seven and special attention is paid on dissolution constants that generate very peaky {111} facets on a narrow angular sector.

4 Simulation of etch pits

All shapes of etch pits are calculated introducing the database called New Law in the self elaborated simulation tool TENSOSIM. To simulate etch pits it is assumed that the starting contour of the mask defect exhibit a simple shape. In the following circular and square contours are primarily selected.

4.1 The simulator tool TENSOSIM

The framework of the simulator is the analytical and continuum description of the anisotropic etching of crystals presented in section 3.1. The anisotropy is taken into account through the dissolution constants (database) and the main foundation of the simulator remains independent to the crystal and to the etchant into consideration. Starting data are the database, the wafer orientation, the contour of mask layout and the etching duration t. The flow chart of the simulation is given in Figure 9a. It is composed of six major steps. In step 1 we decompose the starting surface in successive surface elements and the procedure of introduction of these surface elements depends on the nature concave or convex of the successive intersections of the mask contour. These surface elements cut successive vertical planes P_{Vi} along surface profiles composed of linear elements. So in step 2 we calculate the displacements $\mathbf{P_i}$ of all profile elements potentially present at mask edges that lie in successive cross sectional planes P_{Vi}. At this point the surface profile S_i obtained in a plane P_{Vi} shows crossings (Figure 9b). So tests are made in step 3 to eliminate these unphysical crossings. In step 4 we calculate the intersection points I_{ij} of previous surface profiles S_i in successive horizontal planes P_{Hj}. We thus obtain constant level contours C_j in which crossings can be observed. The elimination of these crossing by specific tests is performed in step 5. Finally

with this procedure the final etching shape of a micromachined structure is furnished in the form of a constant level contour diagram.

4.2 Simulations

Firstly let us suppose that the mask defect has a circular contour. The simulator gives the theoretical predictions shown in Figure 10 for (hk0) planes and in Figure 11 for (hhℓ) planes. Turning attention to Figure 10 we observe that the top contour of (010) and (110) etch pits are composed of four and six linear segments respectively showing that planar facets limit pits. It is obvious that the four segments of (010) pits correspond to intersections of the four $(1\bar{1}1)$, $(\bar{1}\bar{1}1)$, $(1\bar{1}\bar{1})$ and $(\bar{1}1\bar{1})$ planes with the upper surface. In the case of the (110) pit the simulator generates (Figure 10d) effectively six {111} facets with four vertical facets in close accord with experimental observation (Figure 4e). Figure 10 illustrates conveniently how when the angle φ varies from 0° to – 45° the starting four {111} facets are progressively transformed into six {111} facets whose inclination changes progressively. The agreement between experimental shapes and theoretical shapes is very good for (010), (140) and (110) surfaces. At first sight the (230) pit does not look as the experiment etch pit. However with a careful examination we recognize in Figure 10c the contour elements LS_1 and LS_2 and symmetrical ones present in Figure 4d.

In Figure 11 we follow the theoretical evolution of etch pit when the angle θ falls from 90° ((001) surface) to 0° ((110) surface). A decrease of 10° in starting angle θ (θ = 90°) induces a significant change in the etch pit shape. Effectively the final shape of (118) pit (Figure 10b) differs from the well known (001) pyramidal shape. Figure 11 gives also evidence for a transition in etch pit shape that occurs for the (111) surface (θ ≅35°). It is sufficient to compare Figures 11e with Figure 11f corresponding to (112) and (221) pits respectively. Moreover in the case of (hh1) etch pits (Figures 11f to 11i) the more marked changes in shape with decreasing θ appears to be the slow evolution in inclination of f_{O1} and f_{O2} limiting facets.

Figures 12 and 13 show theoretical shapes of etch pits in the special case of a square mask defect. Etching times were adjusted for the various (hhℓ) surfaces in order to derive etch pits bordered by {111} facets only. As expected {111} facets develops and propagate at the four square corners of the mask. Let us recall that the $[1\bar{1}0]$ direction lies in (111) and f_{O2} ($(11\bar{1})$ or $(\bar{1}\bar{1}1)$) limiting planes. So these two limiting planes are rapidly formed at corners whereas the four other {111} limiting facets develops progressively. As a result the two (111) and f_{O2} limiting facets cut the upper surface along two linear segments LS_1 and LS_4 (see Figure 13f for the definition of segments LS_i) that are the most longer of the top contour. The difference between lengths of intersecting segments LS_1 and (LS_2, LS_3) is more marked for (hh1) pits (Figure 13) than for (11ℓ) pits (Figure 12). In contrast in the case of a circular mask (Figure 11) the six {111} facets are tangent to the starting mask contour. This means less difference in the length of the six segments LS_i that compose the contour of (hhℓ) pits. Comparison of Figures 11g, 11h and 11i with Figures 13a, 13b and 13c conveniently illustrates the influence of starting mask contour on the final contour of etch pit. In view of theoretical results fitted in Figures 11 and 13 and provided that pits are only limited by {111} facets we can conclude that changes in the shape of mask contour affect only the length of intersecting segments LS_i.

At this point it is interesting to investigate the influence of a misalignment of the square mask with respect to the standard $[1\bar{1}0]$ direction on the final shape of (hhl) etch pits. Figure 14 shows theoretical (112) and (441) etch pits as derived assuming misalignments of few degrees. Clearly the mirror symmetry is destroyed and the simulator generates pairs of

segments (LS_2,LS_2*) and (LS_3,LS_3*) with different lengths. Simulated etch pits as shown in Figures 14a and 14b are quite successful for the experimental etch pits of Figures 3A and 6c respectively. Moreover let us pay attention to (112) etch pits of Figures 3a and 3A. Taking into account above arguments it is reasonable to assume that pits of Figures 3a and 3A are the result of clockwise and anticlockwise misalignments respectively. In conclusion it can be seen that a misalignment does not affect the nature of limiting facets but has a marked influence on the final top contour of etch pits.

As {111} planes dissolve very slowly for all etchants investigated in this study the final etching shape of small etch pits does not depend on the etchant. This property remains true until the duration of etching leads to the formation of {111} facets only. For shorter etching durations the independence of pit shape on etchant is no longer valid because facets associated to secondary maxima of the dissolution slowness can also bound pits. In particular {100} planes are known [5,13,22,30] to act as limiting facets for KOH, TMAH and NaOH etchants. The early formation, the subsequent development and finally the disappearance of these {100} facets is determined by the anisotropy ratio k. This ratio takes a value of about 100 for the KOH 35% solution [5,22] and falls to about 20 for the TMAH solution [30]. In addition {110} planes correspond also to protuberances (maxima) of the dissolution slowness surfaces in the case of KOH and to valleys (minima) in the case of TMAH. These differences in etching behaviours justify at *posteriori* the adjustment of the database. With a careful adjustment it becomes possible to follow the development of etch pits with increasing etching durations and to show that for short durations secondary limiting facets participate to etching shapes. Figure 15 illustrates the evolution of etch pit shape with the etching duration for (113) and (230) surfaces immersed in a KOH 35% solution. For short etching time a facet (facet F* in Figures 15a and 15A) other than a {111} facet bound etch pits. In Figures 15b and 15B the etching duration is adjusted to prevent the appearance of this facet F* that is just blocked by {111} facets. As soon as {111} facets limit only etch pits etching shapes are not longer modified by prolonged etching (compare Figures 15b and 15B with Figures 15c and 15C respectively). Let us recall for the KOH etchant the dissolution slowness ratio $L_{\{110\}}/L_{\{100\}}$ is close to .5 so that in terms of dissolution criteria [2] etch pits are primarily bounded by {111} facets and secondarily by {100} facets. The observation of {110} facets is highly improbable. The F* facet in Figure 15a intersects the reference (113) surface along the $[1\bar{1}0]$ direction whereas the F* facet in Figure 15A cuts the (230) surface along the [001] direction. Hence it is reasonable to assume that F* facets are (001) and (010) facets for (113) and (230) etch pits respectively. Moreover careful examination of Figure 5c reveals the presence of a F* facet in agreement with theoretical prediction of Figure 15a. Figure 16 shows results for a "large" pit (more than 100 μm × 100 μm in size). The experimental (551) pit is obtained with a contour mask that deviates from the standard rectangular contour aligned along the $[1\bar{1}0]$ direction. Together with usual {111} facets the etched pit is bounded with two other facets identified as facets F1 and F1* in Figure 16a. One can easily depict in Figure 16a the bottom (551) surface covered with dissolution figures like grooves aligned along the $[1\bar{1}0]$ direction. The theoretical (551) pit of Figure 16b is composed of eight limiting facets and with a long rectangular mask the simulator yields elongated symmetrical F1 and F1* facets that correspond well with the two additional facets identified in Figure 16a. So compared with experimental etching shapes, the simulated shapes of Figures 15 and 16 show the interest to perform an accurate adjustment of the dissolution constants.

In addition values of the lateral extent K_{LE} as estimated from the theoretical diagrams of Figures 11, 12 and 13 are also collected in Table 3. This table reveals that the agreement between theoretical values calculated from geometrical considerations and values furnished by simulations is very good for (11ℓ) pits with deviations less than 3 %. More marked

departures are observed for (hh1) etch pits. Effectively the departure reaches about 10 % for most of (hh1) pits (the (221) pit excepted). The theoretical formation of a slightly curved (111) facet instead of a perfectly planar facet (see Figure 13 for example) explains the observed discrepancies.

5 Conclusions

The formation of etch pits on various singly and doubly rotated silicon surfaces is studied. For long durations of etching small etch pits are exclusively bordered by {111} facets making final 3D etching shapes independent on the nature of etchants. This independence is not still valid for short durations or large etch pits.

The orientation dependence of final 3D etching shapes of etch pits is investigated using the kinematic and tensorial model of the anisotropic dissolution. The simulator TENSOSIM that is based on the KT model generates theoretical shapes close to experimental shapes for small (hk0) and (hhℓ) etch pits. The simulator gives also a fair description of the influence of mask misalignment and of etching duration on etching shapes. It is also found that for a given etchant and for large etch pits the simulator furnishes good etching shapes provided the database specific to the etchant was accurately adjusted. Thus it is concluded that the KT model and correlated simulations satisfactory account for micromachining of (hk0) and (hhℓ) pits even when only blocking facets are active. Let us recall that micromachined mechanical structures may be partly composed of regions with blocking facets. So the simulator TENSOSIM appears to be a convenient tool for the study of such blocked regions.

References

1. J. Korvink, O. Paul, *MEMS: A Practical Guide of Design, Analysis and Application*, (William Andrew, Norwich, NY, 2006)
2. K. Sangwal, *Etching of Crystals*, (North Holland, Amsterdam, 1987)
3. K.E. Petersen, Proc. IEEE, **70**, 420 (1982)
4. H. Seidel, L. Csepregi, A. Heuberger, H. Baumgärtel, J. Electrochem. Soc., **137**, 3612 (1990)
5. C.R. Tellier, J. Mater. Sci., **33**, 117 (1998)
6. U. Schnakenberg, W. Beneke, B. Lochel, Sens. Actuators A, **21-23**, 1031 (1990)
7. I. Zubel, Sens. Actuators A, **70**, 70 (1998)
8. K. Sato, M. Shikida, T. Yamashiro, K. Asaumi, Y. Iriye, Sens. Actuators A, **73**, 131 (1999)
9. O. Tabata, Sens. Actuators A, **53**, 250 (1996)
10. C.R. Tellier, A.R. Charbonnieras, Sens. Actuators A, **105**, 62 (2003)
11. A. Merlos, M. Acero, M.H. Bao, J. Esteve, Sens. Actuators A, **37-38**, 250 (1993)
12. C. Hodebourg, C.R. Tellier, Active Passive Electron. Components, **24**, 31 (2001)
13. C. R. Tellier, C. Hodebourg, S. Durand, Active Passive Electron. Components, **24**, 243 (2002)
14. R.B. Heimann in *Silicon Chemical Etching* edited by J. Grabmaier (Springer, Berlin, 1982)
15. H.M. Cuppen, E. van Veenendaal, J. Van Suchtelen, W.J.P. van Enckevort, E. Vlieg, J. Cryst. Growth, **219**, 165 (2000)
16. E. Van Veenendaal, K. Sato, M. Shikida, A.J. Nijdam, J. Van Suchtelen, Sens. Actuators A, **93**, 233 (2001)
17. E. Van Veenendal, *From an atomistic to a continuum description of crystal growth. Application to wet etching of silicon,* Ph.D. thesis, University of Nijmegen, 2001
18. C.R. Tellier, S. Durand, Sens. Actuators A, 60, 168 (1997)
19. C.R. Tellier, C. Hodebourg, T.G. Leblois, Active Passive Electron. Components, **26**, 95 (2003)
20. C.R. Tellier in *Proceedings of the IEEE Sensors Conference, Vancouver, 2003,* (IEEE, CD-ROM, 2003) p 517
21. T.R. Meeker, *IEEE Standard on Piezoelectricity*, (ANSI/IEEE Std 176, 1987)
22. M. Shikida, K. Tokoro, D. Uchikawa, K. Sato, J. Micromech. Microeng., **10**, 522 (2000)
23. C.R. Tellier, J. Cryst. Growth, **96**, 450 (1989)
24. C.R. Tellier, J.L. Vaterkowski, J. Mater. Sci., **24**, 1077 (1989)
25. F.C. Frank, M.B. Ives, J. Appl. Phys., **31**, 1996 (1960)
26. M.J. Lighthill, G.B. Whitman, Proc. Roy. Soc. A, **229**, 317 (1955)
27. C.R. Tellier, D. Benmessaouda in *Proceedings of the 8th European Frequency and Time Forum, Munich,* (VDI Projekt, Dusseldörf, 1994) p 245
28. T.G. Leblois, C.R. Tellier, J. Phys. III France, **2**, 1259 (1992)
29. C.R. Tellier, A. Brahim Bounab, J. Mater. Sci., **29**, 5993 (1994)
30. A.R. Charbonnieras, C.R. Tellier, Sens. Actuators A, **77**, 81 (1999)
31. M. Sato, M. Shikida, Y. Matsushima, T. Yamashiro, K. Asumi, Y. Iriye, M. Yamamoto, Sens. Actuators A, **64**, 87 (1998)

Captions to figures

Figure 1: Etch pits formed on (100) surfaces. Images **a**, **b** are for NaOH 35% and TMAH 25% etchants respectively

Figure 2: Resemblance of shapes for etch pits formed on (hk0) surfaces. Images **a**, **A** are for (110) surfaces and TMAH 25% and KOH 35% etchants respectively. Images **b**, **B** are for (140) surfaces and NaOH 35% and KOH 35% etchants respectively. The arrow in Figure 2a indicates the [001] direction.

Figure 3: Resemblance of shapes for etch pits formed on (hhℓ) surfaces. Images **a**, **A** are for (112) surfaces and KOH 35% and NaOH 35% etchants respectively. Images **b**, **B** are for (661) surfaces and KOH 35% and NaOH 35% etchants respectively

Figure 4: Evolution of shapes with orientation for etch pits formed on (hk0) surfaces. Images **a**, **b**, **c**, **d** and **e** are for (010), (160), (140), (230) and (110) surfaces respectively. Etch pits in images **b**, **c**, **d** and **e** are obtained with a KOH 35 % etchant. Etch pit in image **a** is for a TMAH solution. Arrows indicate the rotated x'_1 direction.

Figure 5: Evolution of shapes with orientation for etch pits formed on (11ℓ) surfaces. Images **a**, **b**, **c** and **d** are for (118), (114), (113) and (112) surfaces respectively. Etch pits in images **c** and **d** are obtained with a KOH 35 % etchant. Etch pits in images **a** and **b** are for TMAH and NaOH solutions. Arrows indicate the rotated <110> direction (x'_1 direction).

Figure 6: Evolution of shapes with orientation for etch pits formed on (hh1) surfaces. Images **a**, **b**, **c** and **d** are for (221), (331), (441) and (661) surfaces respectively. Etch pits in images **a, b** and **C** are obtained with a NaOH 35 % etchant. Etch pits in images **d** are for a KOH 35 % Solution. Arrows indicate the rotated <110> direction (x'_1 direction).

Figure 7: Micromachining of membranes and mesas on (hk0) surfaces. SEM images **a** and a* are for (370) and (230) surfaces respectively. Diagrams **b** and **b*** were derived in a previous work using the Law 1. Diagrams **c** and **c*** are obtained with the new database (New Law).

Figure 8: Micromachining of a mesa on a (140) surface. SEM image (**a**) and theoretical shapes as derived with the previous database (**b**) and with the new database (**c**).

Figure 9. The flow chart of the simulation (**a**) and cross sectional etch path with crossings (**b**).

Figure 10: Simulated shapes for etch pits formed with a circular mask. Diagrams **a**, **b**, **c** and **d** are for (010), (140), (230) and (110) surfaces respectively.

Figure 11: Simulated shapes for etch pits formed with a circular mask. Diagrams **a**, **b**, **c**, **d**, **e**, **f**, **g**, **h**, and **i** are for (118), (115), (114), (113), (112), (221), (331), (441) and (661) surfaces respectively.

Figure 12: Simulated shapes for etch pits formed on (11ℓ) surfaces with a starting square mask. Diagrams **a**, **b**, **c**, **d** and **e** are for (118), (115), (114), (113) and (112) surfaces respectively.

Figure 13: Simulated shapes for etch pits formed on (hh1) surfaces with a starting square mask. Diagrams **a**, **b**, **c**, **d** and **e** are for (331), (441), (551), (661) and (110) surfaces respectively.

Figure 14: Influence of misalignment ψ. Diagrams **a** and **b** are for (112) surface with ψ = 3° and (441) surface with ψ=5° respectively. The linear segment LS_i are identified in schematic diagram **c**.

Figure 15: Influence of the etching duration t (in arbitrary unit) on (113) and (230) surfaces.

Figure 16: SEM image (**a**) of a "large" (551) pit etched in a KOH 35% solution and simulation (**b**) as derived starting with a rectangular mask.

Table 1: Orientation of the various silicon surfaces and corresponding values of angles of cut φ and θ.

(hk0) surfaces		
Crystal surface	Angle φ (°)	Angle θ (°)
(010)	0	0
(160)	– 9.46	0
(140)	– 14.04	0
(230)	– 33.69	0
(110)	– 45	0
(hhℓ) surfaces		
Crystal surface	Angle φ (°)	Angle θ (°)
(118)	– 45	79.97
(114)	– 45	70.53
(113)	– 45	64.76
(112)	– 45	58.17
(221)	– 45	19.47
(331)	– 45	13.26
(441)	– 45	10.0
(551)	– 45	8.05
(661)	– 45	6.72

Table 2: The various etchants. TMAH is for tetra-methyl ammonium hydroxide.

KOH-water	KOH-water	TMAH-water	NaOH-water
35% in weight	54% in weight	25% in weight	35% in weight

Table 3: Experimental and theoretical values of the lateral extent ratio K_{LE}. Values of K_{LE} as estimated from simulated pits are also collected in this table.

Surface	Experiment	Theory	Simulation
(118)	2.14	2.10	2.11
(115)	-	3.5	3.54
(114)	4.97	4.98	5.05
(113)	9.82	10	9.75
(221)	4.83	5	7.5
(331)	2.69	2.8	3.1
(441)	2.09	2.14	2.35
(551)	1.92	1.83	1.97
(661)	1.65	1.65	1.74

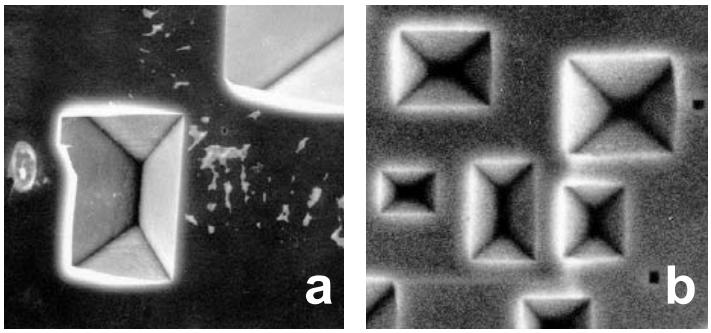

Figure 1: Etch pits formed on (100) surfaces. Images a, b are for NaOH 35% and TMAH 25% etchants respectively

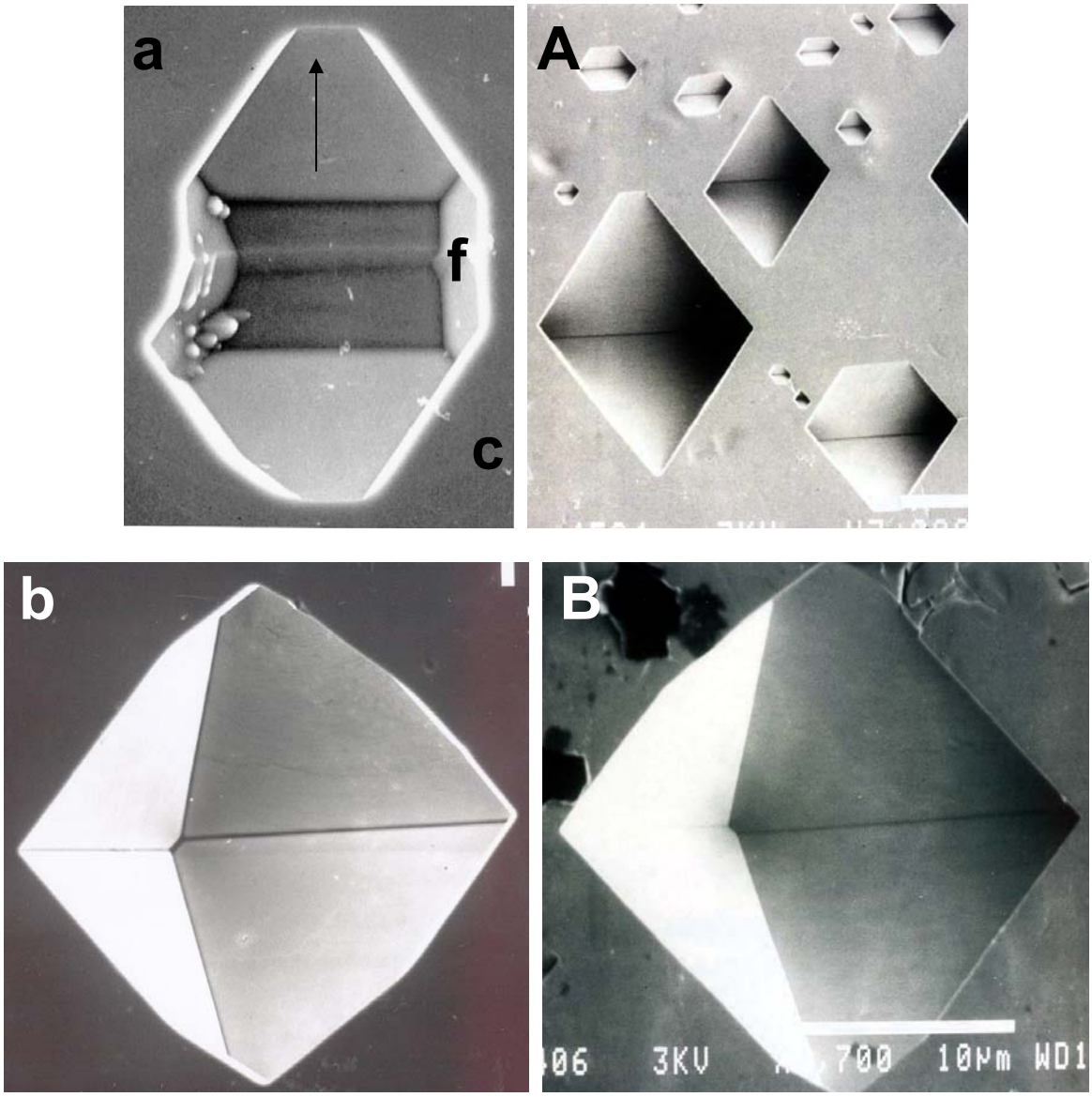

Figure 2: Resemblance of shapes for etch pits formed on (hk0) surfaces. Images a, A are for (110) surfaces and TMAH 25% and KOH 35% etchants respectively. Images b, B are for (140) surfaces and NaOH 35% and KOH 35% etchants respectively. The arrow in Fig. 2a indicates the [001] direction.

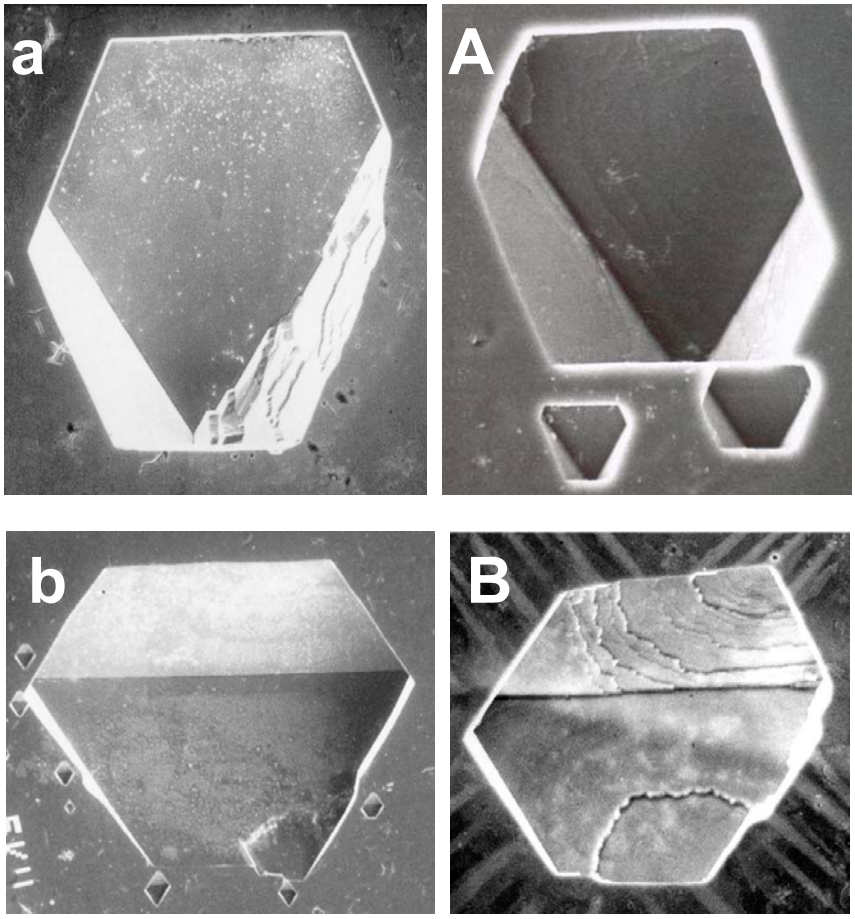

Figure 3: Resemblance of shapes for etch pits formed on (hhℓ) surfaces. Images a, A are for (112) surfaces and KOH 35% and NaOH 35% etchants respectively. Images b, B are for (661) surfaces and KOH 35% and NaOH 35% etchants respectively

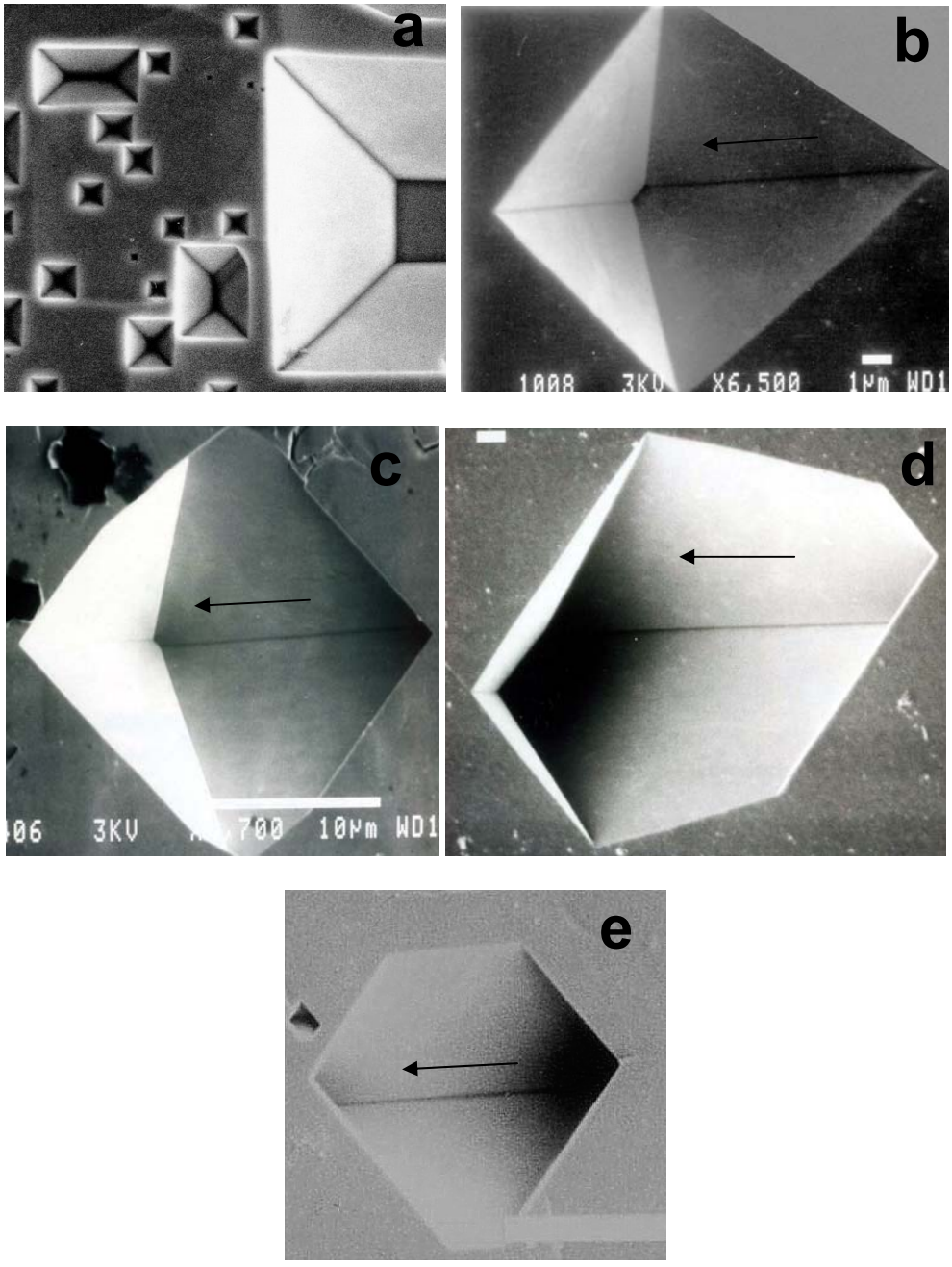

Figure 4: Evolution of shapes with orientation for etch pits formed on (hk0) surfaces. Images **a**, **b**, **c**, **d** and **e** are for (010), (160), (140), (230) and (110) surfaces respectively. Etch pits in images **b**, **c**, **d** and **e** are obtained with a KOH 35 % etchant. Etch pit in image **a** is for a TMAH solution. Arrows indicate the rotated x'_1 direction.

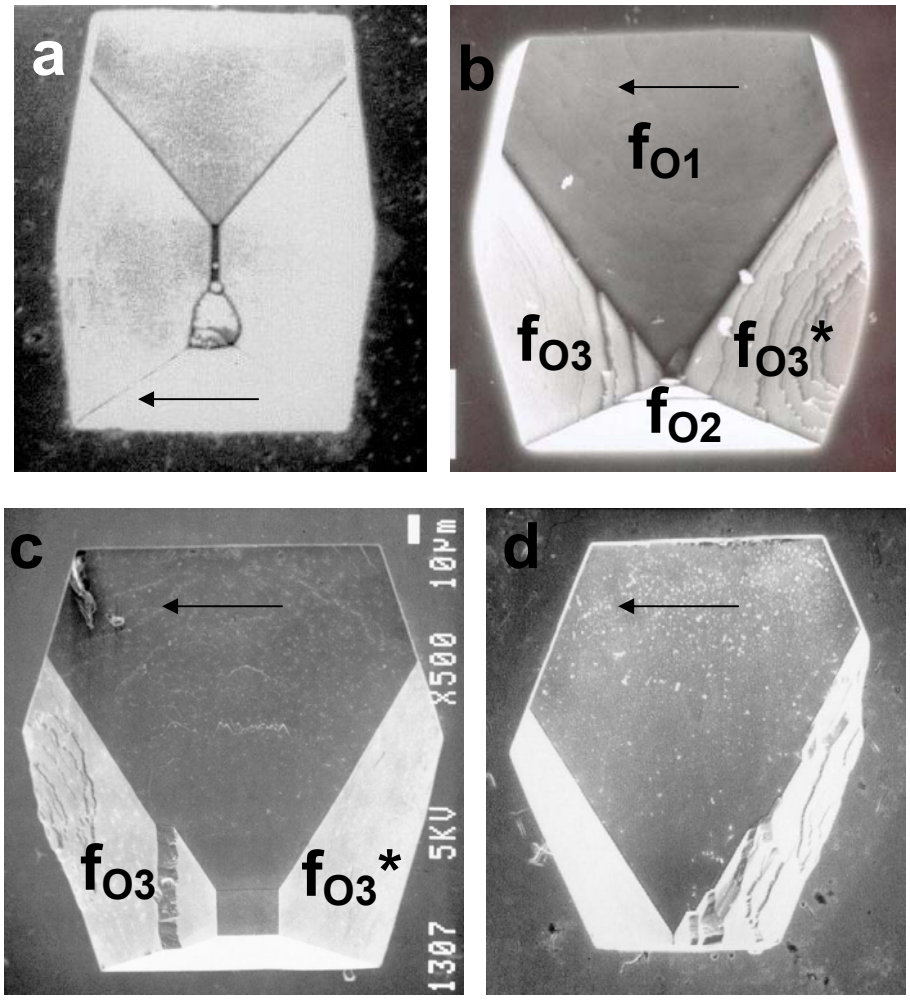

Figure 5: Evolution of shapes with orientation for etch pits formed on (11ℓ) surfaces. Images **a**, **b**, **c** and **d** are for (118), (114), (113) and (112) surfaces respectively. Etch pits in images **c** and **d** are obtained with a KOH 35 % etchant. Etch pits in images **a** and **b** are for TMAH and NaOH solutions. Arrows indicate the rotated <110> direction (x'_1 direction).

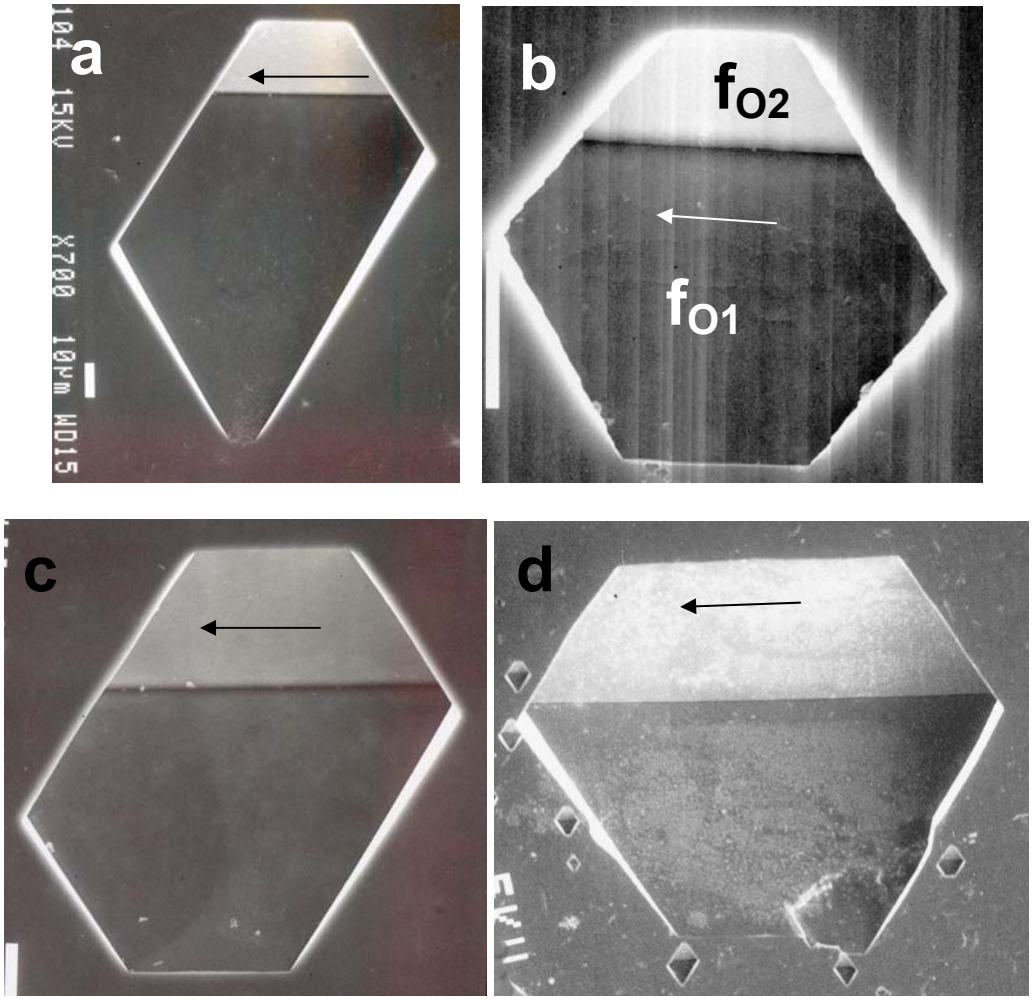

Figure 6: Evolution of shapes with orientation for etch pits formed on (hh1) surfaces. Images **a**, **b**, **c** and **d** are for (221), (331), (441) and (661) surfaces respectively. Etch pits in images **a, b** and **C** are obtained with a NaOH 35 % etchant. Etch pits in images **d** are for a KOH 35 % Solution. Arrows indicate the rotated <110> direction (x'_1 direction).

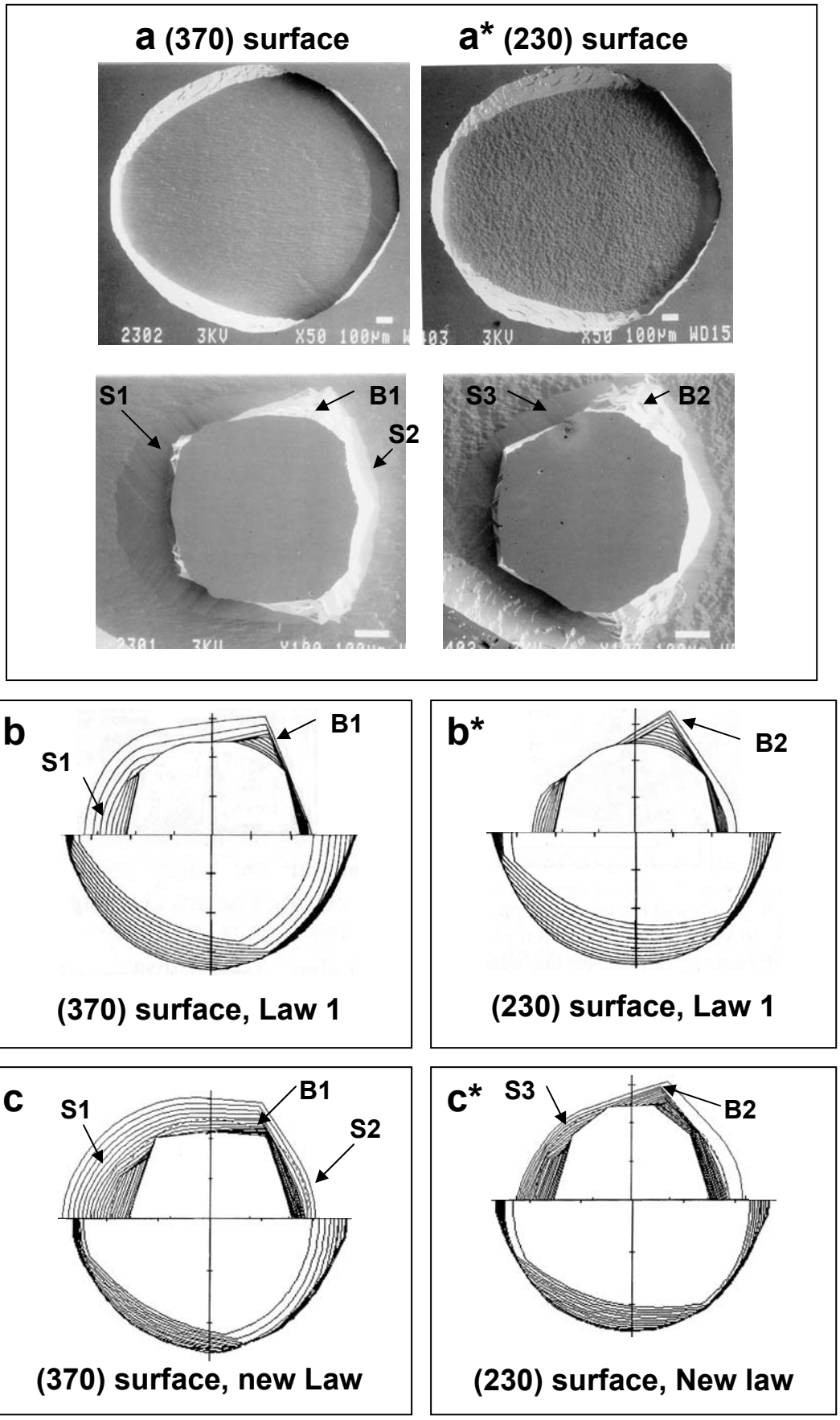

Figure 7: Micromachining of membranes and mesas on (hk0) surfaces. SEM images **a** and **a*** are for (370) and (230) surfaces respectively. Diagrams b and **b*** were derived in a previous work using the Law 1. Diagrams **c** and **c*** are obtained with the new database (New Law).

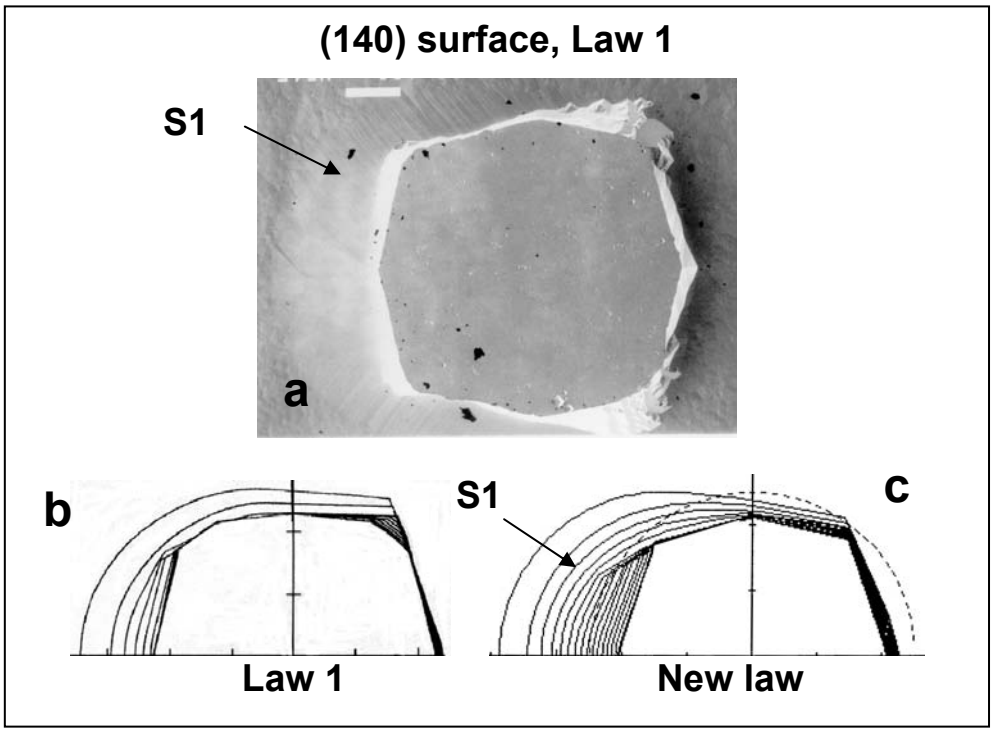

Figure 8: Micromachining of a mesa on a (140) surface. SEM image (**a**) and theoretical shapes as derived with the previous database (**b**) and with the new database (**c**).

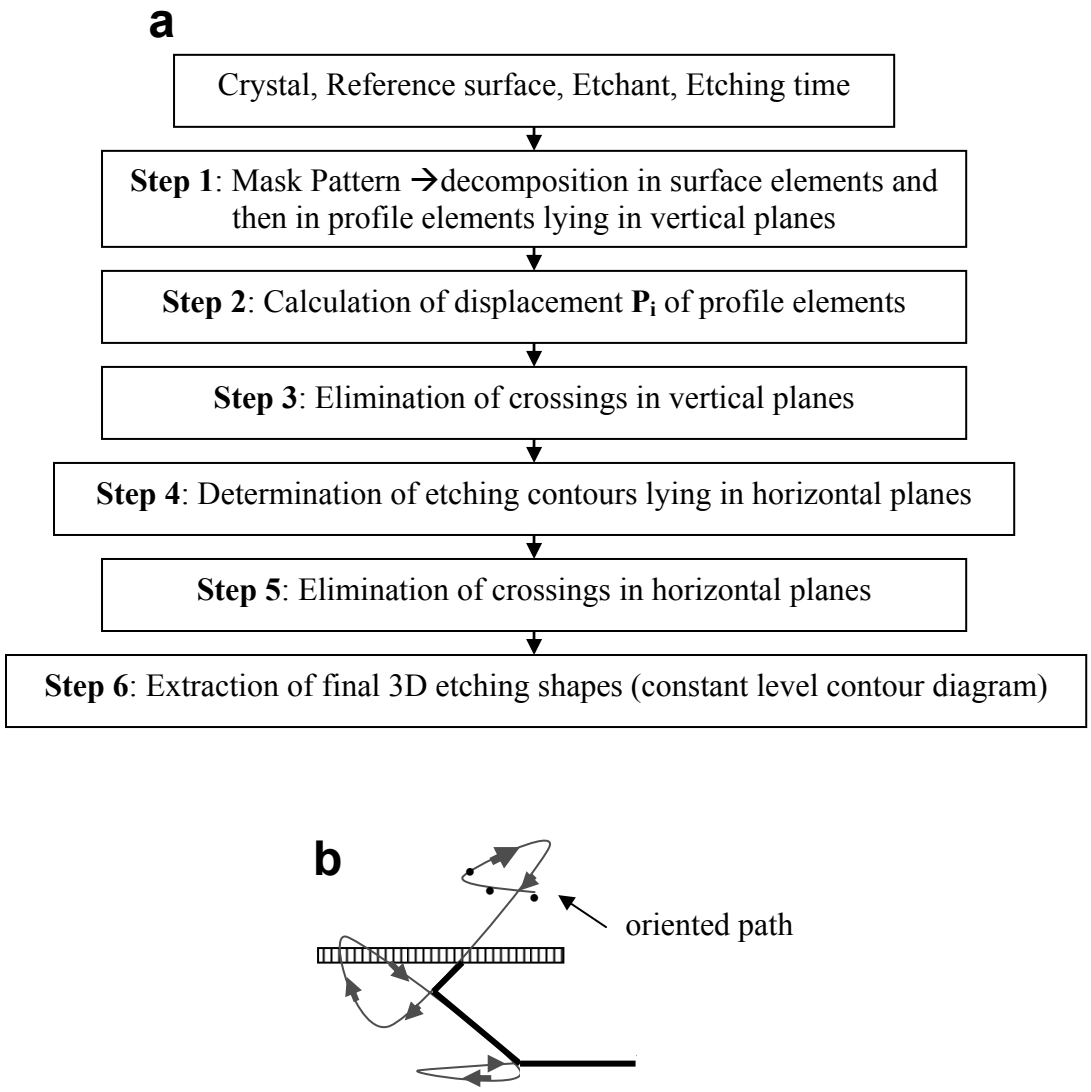

Figure 9. The flow chart of the simulation (**a**) and cross sectional etch path with crossings (**b**).

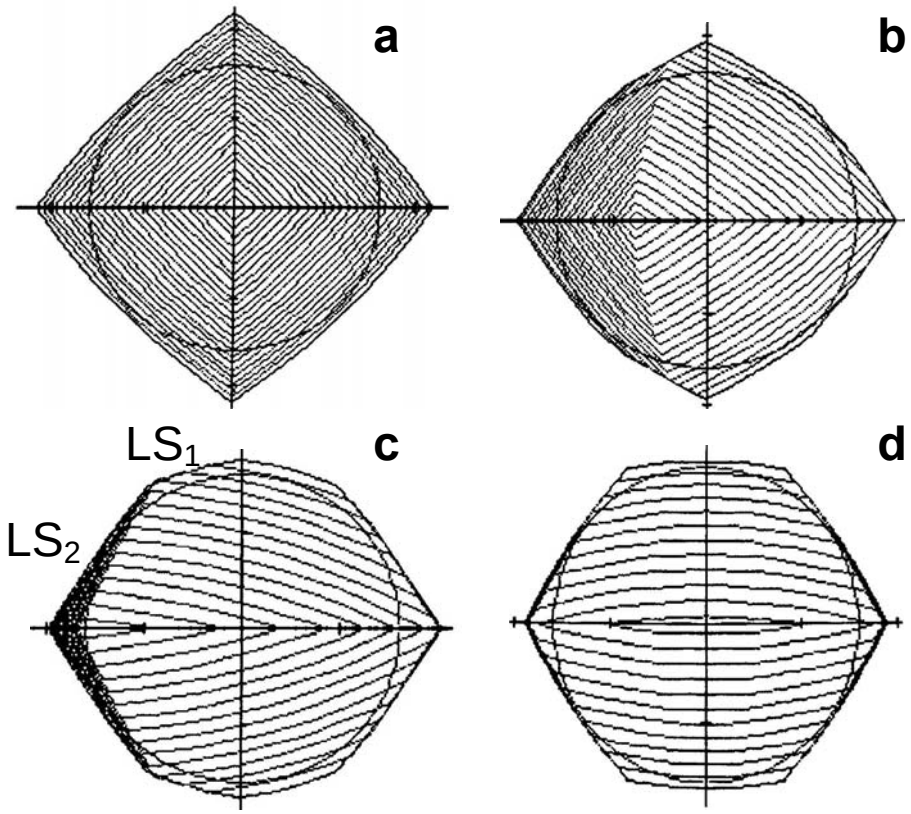

Figure 10: Simulated shapes for etch pits formed with a circular mask. Diagrams **a**, **b**, **c** and **d** are for (010), (140), (230) and (110) surfaces respectively.

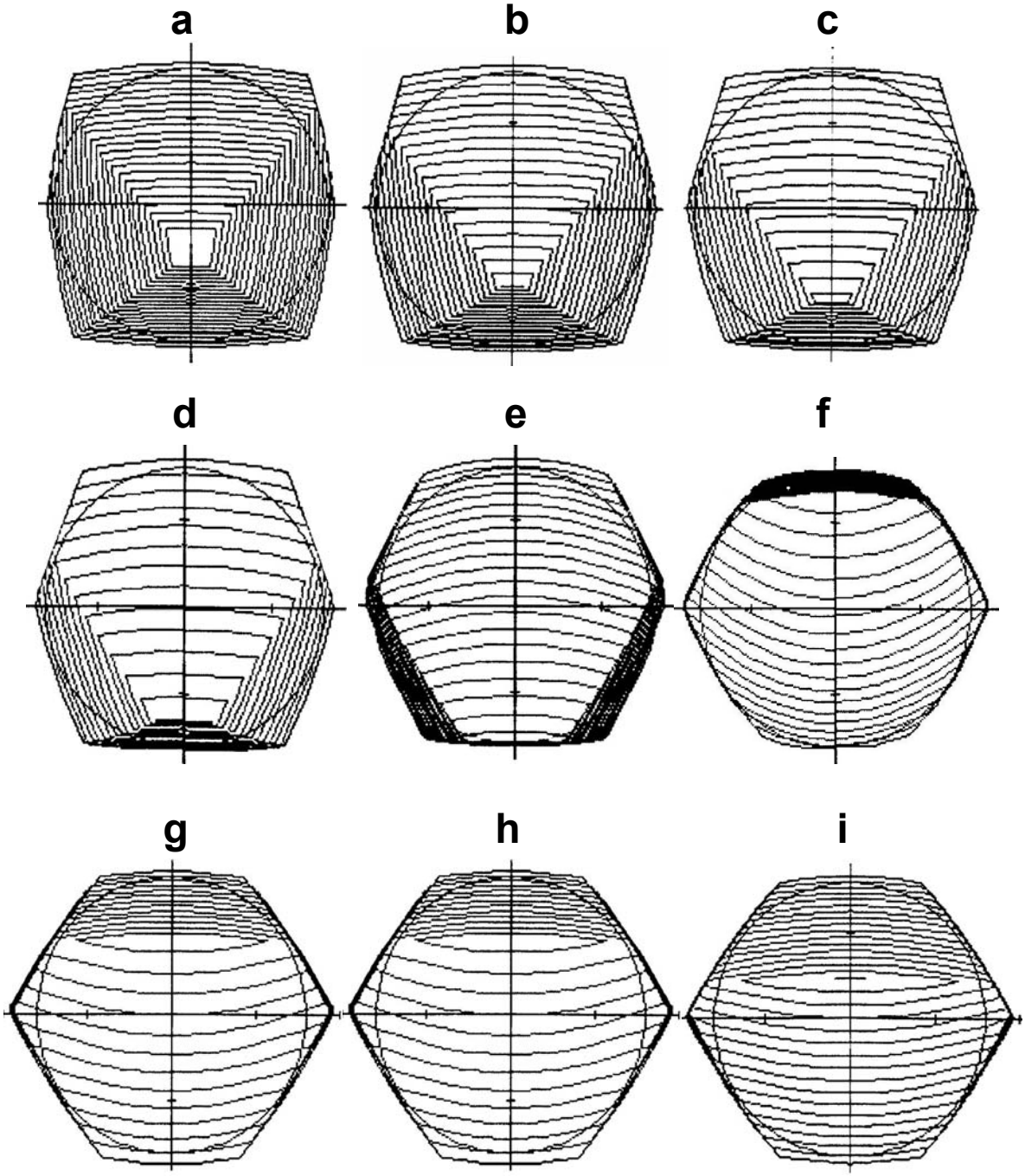

Figure 11: Simulated shapes for etch pits formed with a circular mask. Diagrams **a**, **b**, **c**, **d**, **e**, **f**, **g**, **h**, and **i** are for (118), (115), (114), (113), (112), (221), (331), (441) and (661) surfaces respectively.

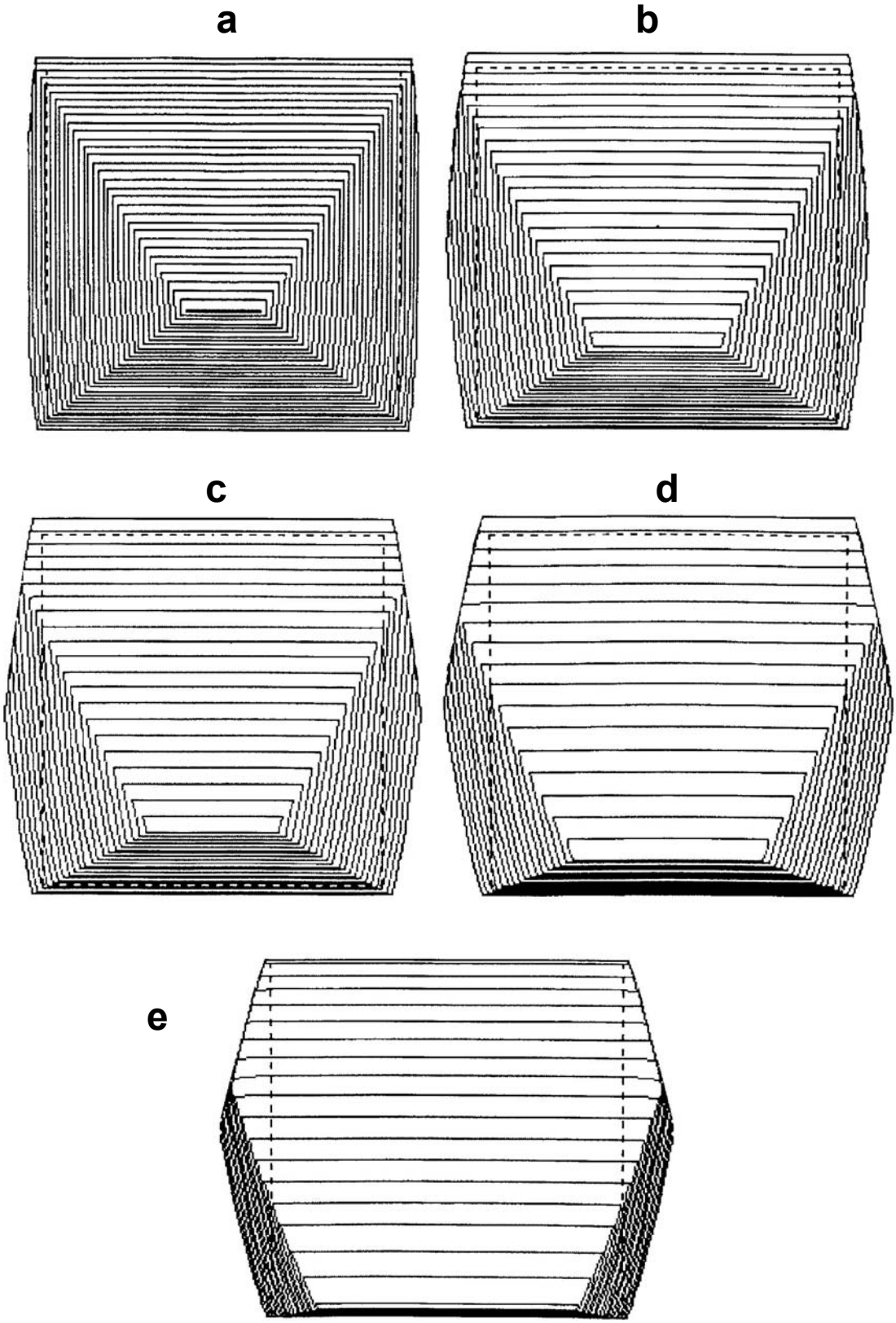

Figure 12: Simulated shapes for etch pits formed on (11ℓ) surfaces with a starting square mask. Diagrams **a**, **b**, **c**, **d** and **e** are for (118), (115), (114), (113) and (112) surfaces respectively.

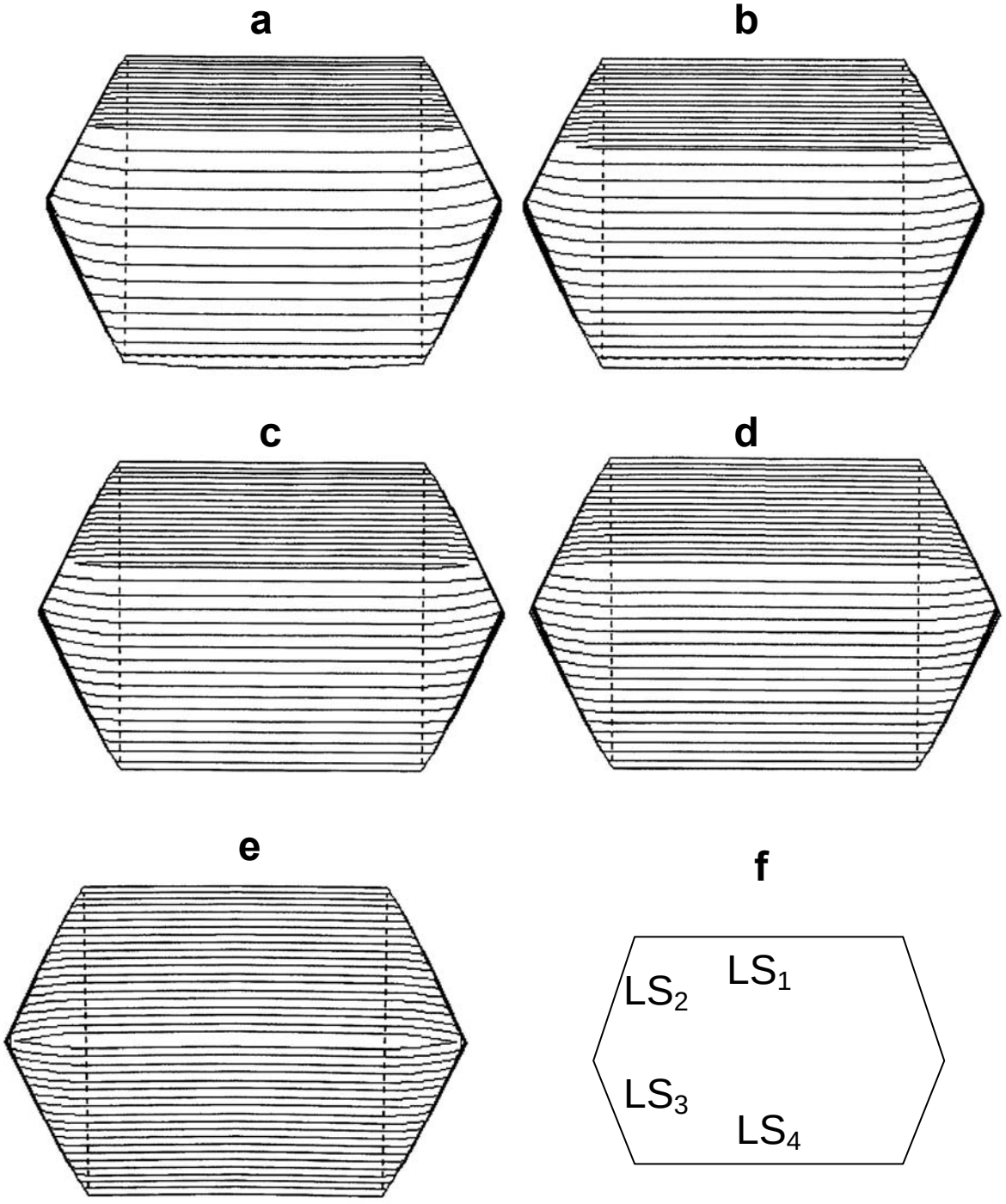

Figure 13: Simulated shapes for etch pits formed on (hh1) surfaces with a starting square mask. Diagrams **a**, **b**, **c**, **d** and **e** are for (331), (441), (551), (661) and (110) surfaces respectively. The linear segment LS_i are identified in schematic diagram **f**.

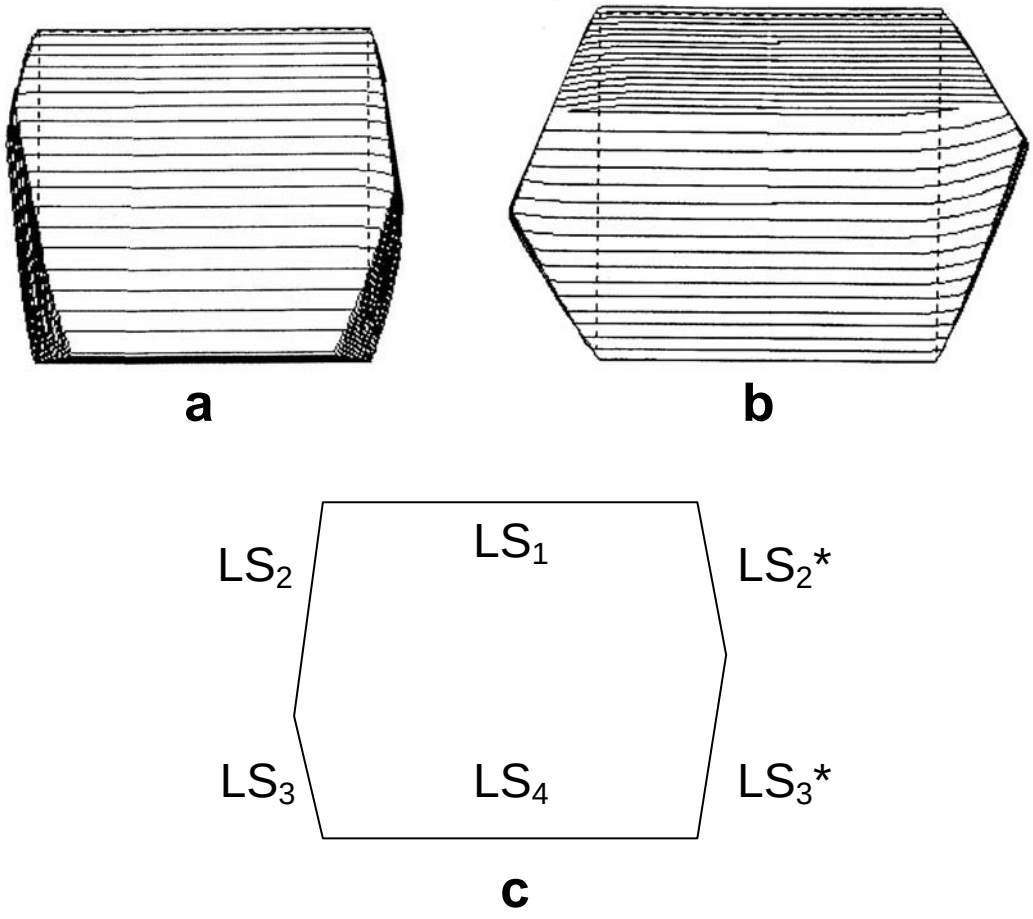

Figure 14: Influence of misalignment ψ. Diagrams **a** and **b** are for (112) surface with ψ = 3° and (441) surface with ψ = 5° respectively. The linear segments LS_i are identified in schematic diagram **c**.

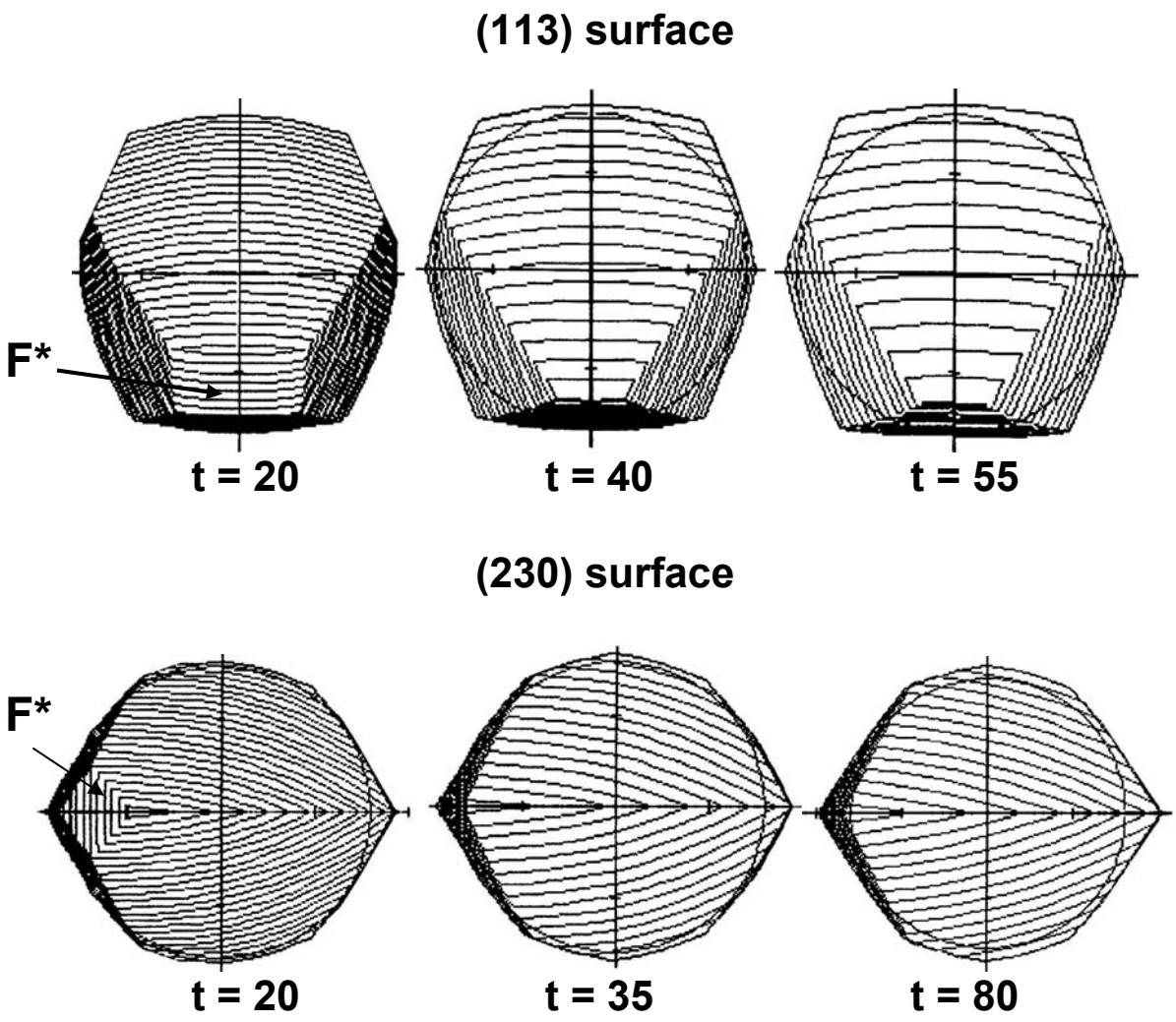

Figure 15: Influence of the etching duration t (in arbitrary unit) on (113) and (230) surfaces.

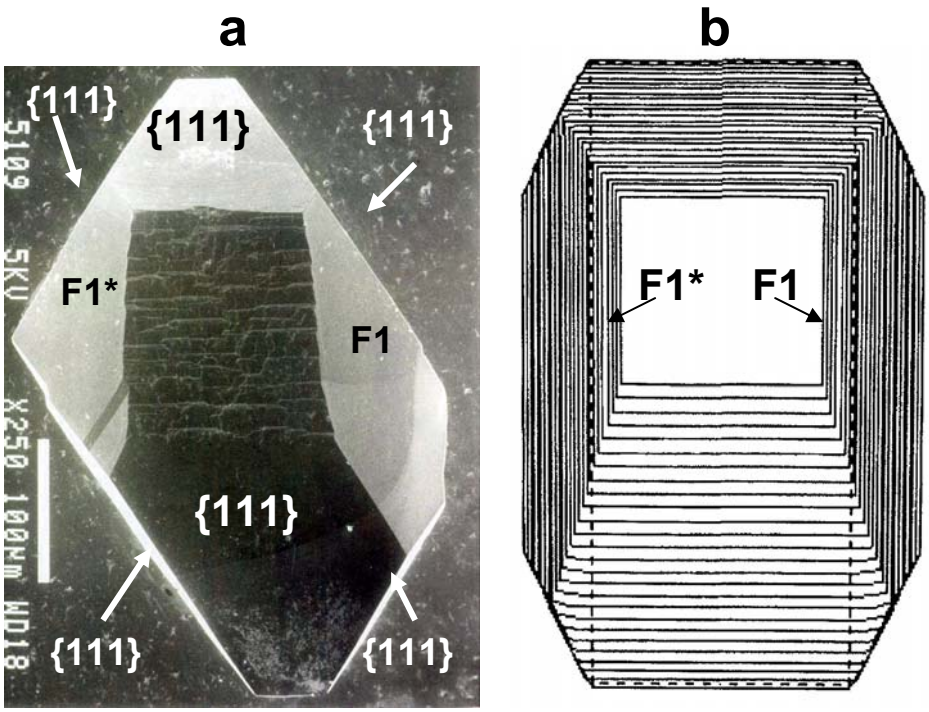

Figure 16: SEM image (**a**) of a "large" (551) pit etched in a KOH 35% solution and simulation (**b**) as derived starting with a rectangular mask.